


 Cite this: *Lab Chip*, 2024, 24, 738

A ddPCR platform based on a microfluidic chip with a dual-function flow-focusing structure for sample-to-result DNA quantification analysis†

 Xiaoliang Zhang,^a Shun Wang,^{‡b} Jinxian Wang,^{‡ab} Xiaojie Sun,^{ab} Jinbing Xue,^b Zhenya Wang,^b Tianhang Yang,^b Liangfei Weng,^c Bidou Wang^{*ab} and Gangyin Luo^{id *ab}

Droplet digital PCR (ddPCR) is a powerful method for absolute nucleic acid quantification with high precision and accuracy. However, complicated operational steps have hampered the use and diffusion of ddPCR. Therefore, an automated, easy-to-use, low-sample-consumption, and portable ddPCR platform is urgently needed. This paper proposes a microfluidic ddPCR platform based on a microfluidic chip that can realize the sample-to-result function by switching the rotary valve, achieving the dual function of the flow-focusing structure for droplet generation and readout. Sample, generation oil, and analysis oil were pre-added to the reservoirs. Droplets were generated due to focusing flow, and after passing through the integrated temporary storage bin in the rotary valve, the droplets and oil subsequently entered the collecting tube, improving the droplet-to-oil volume ratio for enhanced thermal cycle performance. Droplets with an average diameter of 107.44 μm and a CV of 2.38% were generated using our chip under the optimal pressures. High-performance thermal cycling was achieved through improvements of the droplet-to-oil volume ratio of the sample, the integrated heating lid, the pure copper heating base, and the temperature-controlling algorithm. Gradient quantification experiments were conducted for the HER2 and CEP17 genes extracted from breast cancer cells, yielding strong linear correlations with R^2 values of 0.9996 for FAM and 0.9989 for CY5. Moreover, pronounced linearity was obtained between the detected concentrations of HER2 and CEP17, indicated by a slope of 1.0091 and an R^2 of 0.9997, signifying consistent HER2 : CEP17 ratios across various sample dilutions. The outcomes of the quantitative analysis, encompassing the dynamic range and the consistency of the HER2 : CEP17 ratio using our ddPCR platform, meet the standards required for breast cancer assessment and therapy. Our ddPCR platform is automated, portable, and capable of stable droplet generation, high-efficiency amplification, realization of the sample-to-result function based on dual-function flow-focusing structure, and accuracy absolute quantification, underscoring its significant potential for ddPCR analysis in clinical diagnostics.

 Received 15th December 2023,
 Accepted 27th December 2023

DOI: 10.1039/d3lc01078c

rsc.li/loc

Introduction

Digital polymerase chain reaction (dPCR) is a method for the absolute quantification of nucleic acids. Its notable sensitivity and precision make it ideal for detecting rare mutations,

analyzing microsamples, and determining copy number variations.^{1–3} In dPCR, a sample is partitioned into numerous independent units, each theoretically containing no more than one target DNA molecule. After amplification, each unit has two states: ‘0’ (negative) or ‘1’ (positive), depending on its fluorescence intensity.⁴ Absolute quantification of the target DNA molecules can be achieved by counting the negative and positive units and applying the Poisson distribution, without the need for a control group and a standard curve.⁵

The essential step of dPCR is sample partitioning, done either by a chip with microchambers called chamber-based digital PCR (cdPCR), or by creating ‘water-in-oil’ droplets, known as droplet digital PCR (ddPCR).^{6–9} With the rapid development of droplet-based microfluidic (DMF) technique in recent decades,^{10–12} the ddPCR technique has become more

^a School of Biomedical Engineering (Suzhou), Division of Life Sciences and Medicine, University of Science and Technology of China, Hefei 230026, People's Republic of China

^b Suzhou Institute of Biomedical Engineering and Technology, Chinese Academy of Sciences, Suzhou 215163, People's Republic of China. E-mail: wangbd@sibet.ac.cn, luogy@sibet.ac.cn

^c Suzhou Guoke Medical Science & Technology Development Co. Ltd, Suzhou 215163, People's Republic of China

† Electronic supplementary information (ESI) available. See DOI: <https://doi.org/10.1039/d3lc01078c>

‡ These authors contributed equally to this work.

popular than ddPCR. A microdroplet is regarded as a reaction unit in ddPCR. ddPCR has more flexible sample dispensing than microwells and a simpler structural design to form units. Hindson *et al.* generated 20 000 to 200 000 droplets of 1 nL in a microfluidic chip, and up to 1000 droplets could be detected in one second.¹³ Picoliter to nanoliter droplets with a total volume of dozens to hundreds of microliters were generated in one minute in the chip designed by S. H. Zhao *et al.*¹⁴ The ddPCR analysis platform based on DMF offers high throughput, efficiency, and advantages in reagent consumption. Perkins *et al.* designed a ddPCR system to detect KRAS gene mutation.¹⁵ They generated droplets in a microfluidic chip and conducted thermal cycles in a PCR tube. Finally, droplets were transferred to the other chip for fluorescence intensity detection. In this system, experimenters transferred the sample twice, increasing labor costs and the risk of contamination. M. Y. Nie *et al.* designed a microfluidic chip with an emulsification step that could be reused for ddPCR.¹⁶ C. Y. Wei developed another chip with an emulsification step chip for droplet generation.¹⁷ The above researchers have contributed to the ddPCR technology based on microfluidic chips. However, none of them achieved the sample-to-result ddPCR analysis.

Sample-to-result dPCR analysis is typically achieved using two methods, as reported in literature or available commercially. For instance, in the Bio-Rad QX ONE ddPCR system, droplets are generated using a microfluidic chip and then amplified in a PCR tube, similar to our study. However, this system employs a sampling needle during the fluorescence readout process. In this process, droplets are extracted from the PCR tube, drawn into a capillary, and then excited by a laser for fluorescence signal collection. This method boasts the advantage of a high signal-to-noise ratio. However, it requires a significant amount of analysis oil to clean the needle and tubing, and the repeated use of these components may lead to contamination. Furthermore, the use of externally placed consumables introduces additional contamination risks. Additionally, the structure of the optical path and tubes enlarges the platform's dimensions, posing challenges for the design of the multi-sample parallel analysis platform. In the chip developed by Yulin Ren *et al.*,¹⁸ droplets are amplified within a flat chamber, followed by the capture of fluorescence intensity through direct imaging. This chip boasts a simple structure and high throughput. However, it has several drawbacks. An immense pressure of 1500 mbar is required to keep the droplet stable during flat chamber amplification. In other chips, inlets and outlets are sealed with oil.¹⁹ This step was complex for achieving sample-to-result targets. To prevent droplet overlap for image recognition, the chip's thickness is typically less than the diameter of the droplets, resulting in squeezed droplets that are relatively unstable during amplification. Images of droplets were captured by a CMOS or CCD camera. Then, the image recognition algorithm was used to obtain the fluorescence intensity of the droplets after amplification.^{20,21} Nevertheless, image stitching and chip flatness could lead to

errors in droplet recognition, and limited excitation light power results in a low signal-to-noise ratio (SNR) compared to the Bio-Rad ddPCR system.²²

An automated ddPCR platform based on a microfluidic chip integrates droplet generation, amplification, and readout, enabling the sample-to-result function. It can reduce labor, reagent, time, and sample costs. Meanwhile, ddPCR analysis in a microfluidic chip reduces the risk of contamination. Moreover, the automated analysis process with program control is more standardized. In this paper, we developed a portable ddPCR platform measuring 320 × 240 × 220 mm and a microfluidic chip that integrates droplet generation, amplification, and fluorescence readout. We achieved the sample-to-result ddPCR analysis on a single chip, where a dual-function flow-focusing structure is implemented *via* a rotary valve. We used on-chip microchannels instead of common fluidic tubes and pre-integrated consumables into the chip to enable one-key analysis and minimize contamination. Within the chip, an integrated rotary valve is utilized to alter fluid flow directions, facilitating droplet generation *via* forward flow and on-chip fluorescence readout through reflux. Additionally, the chip's dual-function flow-focusing structure reduces its dimensions, thereby benefiting the design of the multi-sample parallel analysis platform. Furthermore, a compact readout module and a customized thermal cycler, designed specifically for the ddPCR platform, facilitates the miniaturization and portability.

We investigated the size consistency of the droplets, the generation frequency, the droplet-to-oil volume ratio, and the impact of the temporary storage bin on the droplet-to-oil volume ratio in the ddPCR platform. The effect of surface treatment on droplet size and consistency has also been investigated. Four optimizations improved the thermal cycle performance. First, a temporary storage bin is incorporated into the rotary valve to increase the droplet-to-oil volume ratio in the collecting tube. Second, an integrated heating lid is used to reduce droplet evaporation. Third, high thermal conductivity pure copper is used to manufacture the heating base. Fourth, the Smith predictor and sensor calibration are added to optimize the temperature-controlling algorithm. The confocal laser-induced fluorescence (LIF) technique is used in our ddPCR platform to achieve a highly sensitive and high signal-to-noise ratio fluorescence signal during readout. Accurate illustration of HER2 characteristics is a critical precondition for evaluating the prognosis and predicting the efficacy of anti-HER2 therapy.²³ We assessed platform performance using gradient quantification assays for HER2 and CEP17 gene concentrations extracted from breast cancer cells.

Material and methods

Reagents

We used a 2% v/v 1H,1H,2H,2H-perfluorodecyltriethoxysilane (FOTS) solution (P122385, Aladdin, China) dissolved in

engineered fluid (Novec 7500, 3M, USA) as a hydrophobic agent for microchannel surface treatment.¹⁴ Human breast cancer DNA was isolated from 54 year-old T-47D cells (Procell CL-0228, Procell Life Science & Technology Co., Ltd). HER2 and CEP17 genes were extracted from the cells. The probe and primer were customized by ThermoFisher (ThermoFisher Scientific, USA). The ddH₂O (B541017, Sangon Biotech, China) was purchased from Sangon Biotech Co., Ltd. Droplet generation oil for probes (D9161172A, Bio-Rad, USA) was used in our study. The ddPCR supermix (1863023, Bio-Rad, USA) and the analysis oil (#1863004, Bio-Rad, USA) were purchased from Bio-Rad. The generation oil was used for droplet formation and separation during droplet generation and readout, respectively.

Design of the sample-to-result microfluidic chip

The assembled chip integrates droplet generation, amplification, and readout functions for sample-to-result ddPCR analysis on a single chip. The 3D drawing of the assembled chip is shown in Fig. 1(A). The assembled chip includes three reservoirs, a rotary valve, a collecting tube, a built-in heating lid, and a flat chip. The 400 μ L analysis oil, 200 μ L generation oil, and 200 μ L sample reservoirs were aligned sequentially with the openings on the left side of the chip and fixed to the chip surface using UV adhesive. We used a socket structure similar to a bayonet nut connect (BNC) to tightly press the rotary valve and the flat chip. The BNC housing, the rotary valve, and the locking ring were successively installed on the chip surface. The BNC housing

was fixed to the upper layer of the flat chip through positioning holes using UV adhesive. The compression of the rotary valve was achieved through the elastic deformation of the material by mating a locking ring to the BNC housing, ensuring leakage was avoided. The built-in heating lid was installed on the substrate layer through the positioning hole, and the collecting tube was inserted into the heating lid through the clamping slot. The heating lid was bonded to the chip with the UV adhesive, and a lidless PCR tube (AM12225, USA, ThermoFisher Scientific) was used as the collecting tube clamped into the built-in heating lid. The exploded view diagram of the chip is shown in Fig. 1(B).

Design of the rotary valve. We designed a rotary valve to connect and seal different channels by rotating it to certain angles. It is made of Teflon to ensure smooth rotation. A slot for screwdriver insertion is located at the top of the valve. The internal structure of the rotary valve is presented in Fig. 1(C). A 30 μ L cylindrical temporary storage bin is built into the rotary valve to achieve a higher droplet-to-oil volume ratio. The droplet-to-oil volume ratio (γ_{do}) is defined as follows:

$$\gamma_{do} = V_{td}/V_{to} \quad (1)$$

here, V_{td} represents the total volume of the droplets in the collecting tube, and V_{to} represents the total volume of the oil in the collecting tube. The volume of the liquid can be calculated according to the size of the collecting tube, by taking the photo. A sloping pipeline connects the bottom opening of the rotary valve to the top of the temporary

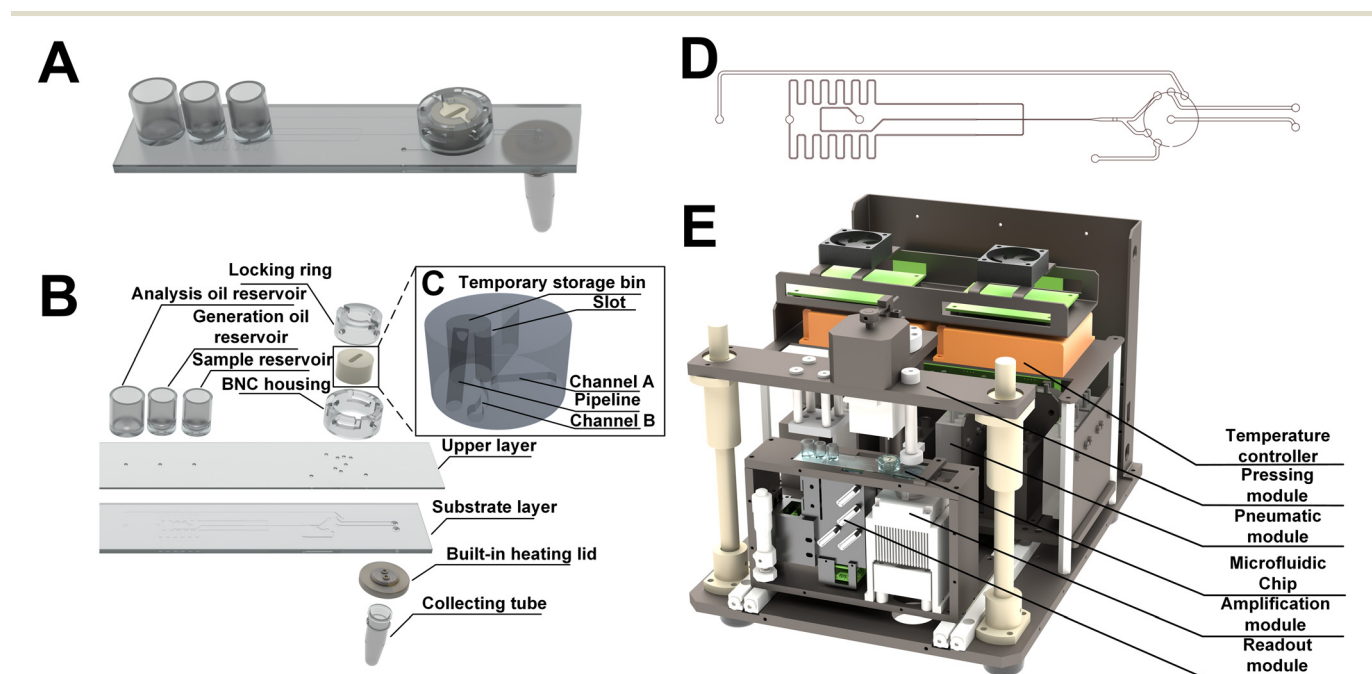


Fig. 1 Schematic diagram of the sample-to-result microfluidic chip and the corresponding experimental device. (A) The 3D diagram of the assembled chip. (B) The exploded view of the chip. (C) The perspective view of the rotary valve. The relative positions of the temporary storage bin, pipeline, channel A, and channel B in the rotary valve are shown. (D) Microchannels and openings in the flat chip. (E) The schematic diagram of the experimental device. The chip is placed in the chip holder.

storage bin. Two channels (A and B) are located on the bottom of the rotary valve. The 3D model and the machining drawings of the rotary valve are available in ESI 2.†

Design of the flat chip. The flat chip was designed using AutoCAD (Autodesk Inc, USA). The flat plate chip comprises an upper layer (0.5 mm thickness) and a substrate layer (1.5 mm thickness) bonded together by thermocompression. The size of the flat chip is $89 \times 20 \times 2$ mm. The microchannels and openings are shown in Fig. 1(D). The chip's upper layer has outlets, inlets, and openings connected to the rotary valve, while the microchannels are located on the chip's substrate layer. Moreover, the substrate layer has two openings used to connect to the heating lid. A dual-function flow-focusing structure was designed for droplet formation during droplet generation, and for droplet separation and arrangement during fluorescence readout by changing the rotary valve angle. The depth and width of the flow-focusing structure were both 70 μm . Furthermore, we designed wider (120 μm) and longer microchannels near the reservoirs to achieve a steady flow velocity.

Design of the built-in heating lid. The air in the upper part of the collecting tube was heated greater than the liquid temperature during amplification. Heating the top plate in the collecting tube does two things. First, this measure increases non-vapor gas temperature and the total pressure in the tube. This increased pressure will increase the boiling point of water, thus avoiding the diverging evaporation rate near the boiling point at 98 °C. Second, it reduces the condensation of the hot vapor to the otherwise colder tube wall. Both of the effects will reduce water loss from the droplets. In addition, the theoretical analysis and experimental verification of the relationship between the evaporation situation and the air temperature are presented in ESI 1.1† and the experimental results are shown in Fig. S1.† In traditional amplification instruments, the heater is placed on the PCR tube lid. However, the heat transfer efficiency is low due to the low thermal conductivity of the collecting tube material. Therefore, in this study, we proposed a built-in heating lid to improve the heating efficiency and temperature stability. Two openings on the lid connect the microchannels in the flat plate chip to the collecting tube.

Experimental platform

The ddPCR platform comprises a portable device and corresponding software installed on a mini computer. The photo of the ddPCR device and the software interface, including its program flowchart, is shown in Fig. S2.† The device is connected to a computer *via* a USB cable. Thus, the ddPCR analysis is automated on our platform under the control of the software. The device includes a pneumatic driving module (containing three independent gas sources), a chip pressing module, an amplification module, two temperature controllers, and a readout module, as shown in Fig. 1(E). They are controlled by the control circuit board. We

designed software for automated ddPCR analysis. After starting the software, the analysis is conducted automatically, and the readout result is displayed when the analysis finishes. The gas source can provide adjustable and stable pressure for driving samples, generation oil, and analysis oil. Different stages of the experiments progressed by switching various pumps and valves. The pressing module, driven by a stepper motor, has three gas vents, a rotary screwdriver, and a spring. When the pressing module goes down, the gas sources come into close contact with the three reservoirs, and the screwdriver is inserted into the slot of the rotary valve. Meanwhile, the spring compresses, ensuring the collecting tube fits closely to the thermal cycler. An annular heater, driven by a temperature controller (TCM207, Yexian Tech, China), is used for the lid heating. A pure copper base is designed for a faster heating-up and cooling-down rate during amplification. The temperature change is achieved using a Peltier (XLT2419, Marlow, USA) driven by a temperature controller (TCM115, Yexian Tech, China). The readout module is exceptionally compact, measuring $79 \times 60 \times 20$ mm and integrates several optical elements, a 488 nm laser diode and a 638 nm laser diode used for fluorescence excitation, and two avalanche photodiode (ADP) detectors (S12023-10A, HAMAMATSU, Japan) mounted on the same side for fluorescence excitation and intensity readout in each droplet.

The procedure of the automated ddPCR analysis

The core of the procedure is realizing the dual-function flow-focusing structure, as shown in Fig. 2(F). This indicates that droplet generation and readout occur in the same flow-focusing structure by forward flow and reflux, respectively. During the ddPCR analysis, pressure was used to determine the onset and completion of droplet generation and reflux readout, respectively. The pressure curves are shown in Fig. S3,† along with the explanations of each pressure variation.

The first step of the analysis is ddPCR sample preparation. The sample volume is 20 μL , containing 1 μL DNA solution, 10 μL ddPCR supermix, 1 μL probe, 2 μL primer, and 6 μL ddH₂O, as shown in Fig. 2(A). Then, the reagents are thoroughly mixed in a vortex mixer for 30 seconds. The rotary valve is rotated to the initial position (+60°), and 20 μL of sample, 180 μL of generation oil, and 300 μL of analysis oil are added to the reservoirs, respectively, following the order in Fig. 2(B). After completing the preparatory work, the chip is placed into the chip holder in the device and secured by the pressing module. The automated droplet generation, amplification, and readout will run according to the program in the software.

At the droplet generation stage (Fig. 2(C)), the rotary valve was turned counterclockwise to the generation position (−30°). Here, channel A connected the collecting tube to the air to maintain pressure balance (with a filter at the outlet to reduce aerosol contamination), and channel B connected the pipeline to the collecting tube. 16 kPa pressure were applied

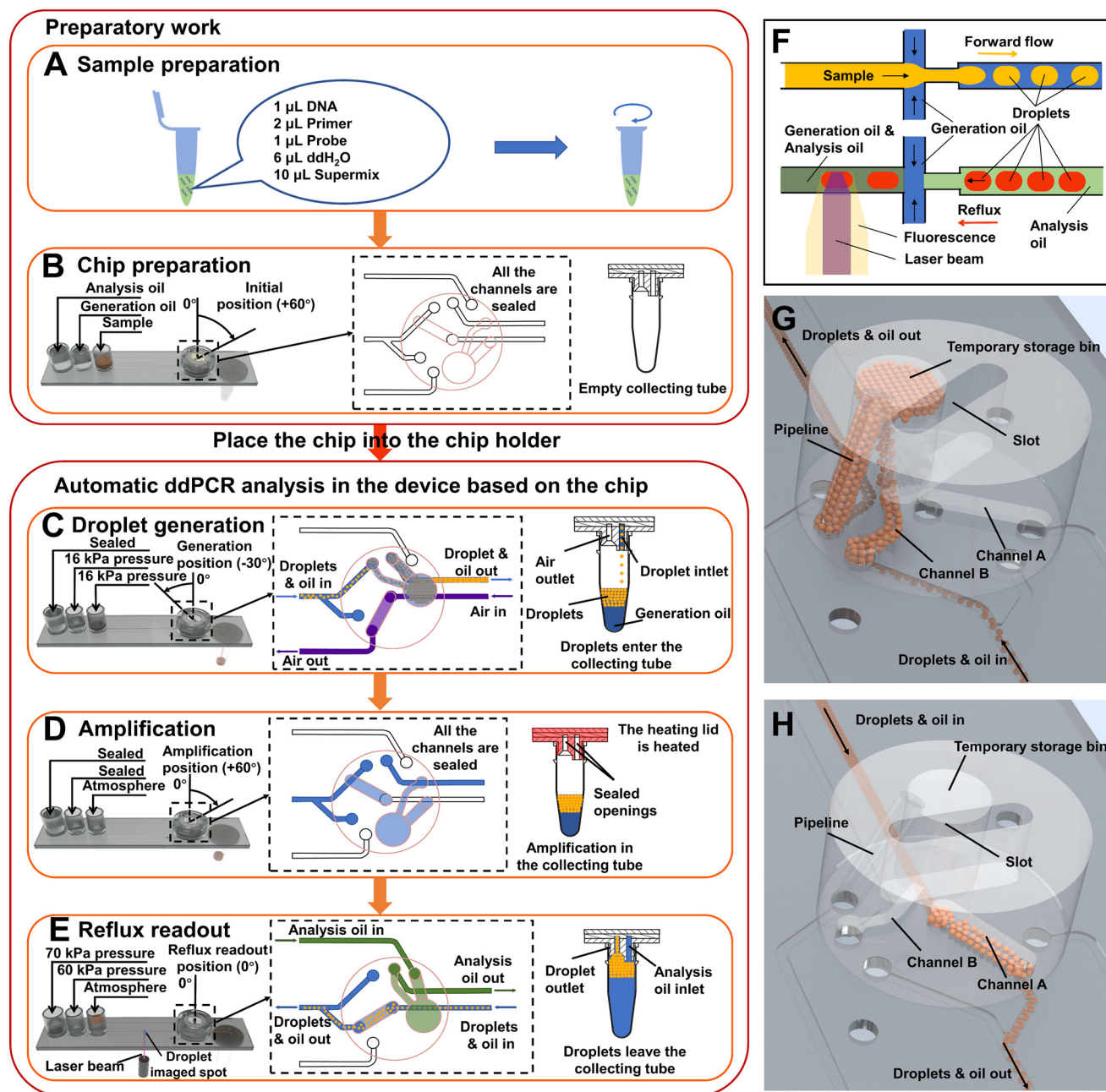


Fig. 2 (A) Sample preparation. (B) The working pattern of the chip during chip preparation. (C) The working pattern of the chip during droplet generation. (D) The working pattern of the chip during amplification. (E) The working pattern of the chip during reflux readout. (F) The principle of the dual-function flow-focusing structure. (G) The schematic diagram of the droplet flow inside the rotary valve during droplet generation. (H) The schematic diagram of the droplet flow inside the rotary valve during reflux readout.

to both the generation oil and the sample, they passed through the flow-focusing structure together, emulsifying the sample and forming uniform-sized droplets due to the focusing flow. As shown in Fig. 2(G), the liquid flow led to the droplets and oil entering the temporary storage bin inside the rotary valve. Due to the lower density of droplets compared to oil, the floating droplets exited the temporary storage bin first and were densely arranged in the microchannels. Finally, the droplets entered the collecting tube. In each experiment, we obtained at least 25 000

droplets. This accounts for various factors, including loss during sample transfer, dead volume of the sample in the reservoir, and the droplets remaining in the microchannels.

During the amplification stage (Fig. 2(D)), the rotary valve was rotated clockwise to the amplification position (+60°), sealing the collecting tube. The heating lid was tightly pressed against the annular heater. The heating lid was heated before the thermal cycle began. This conducted the heat to the inside of the collecting tube, heating the air in its upper part and raising the air temperature to above 100 °C.

The thermal cycles, including 1 cycle of activation (95 °C), 45 cycles of denaturation (94 °C), annealing (55 °C), and extension (65 °C), and 1 cycle of inactivation (98 °C), were conducted in the collecting tube placed in the thermal cycler.

The last stage was the reflux readout. As shown in Fig. 2(E), the rotary valve was rotated counterclockwise to the reflux readout position (0°). In this position, channel A connected the collecting tube to the flow-focusing structure on the flat chip, and channel B connected the analysis oil reservoir to the collecting tube. The sample reservoir was connected to air, with a filter, for pressure balance. During readout, the analysis oil initially entered the temporary storage bin under the pressure of 70 kPa. Subsequently, the analysis oil and generation oil in the temporary storage bin were transferred into the collecting tube, allowing the generation oil to be reused. The droplets floated out of the collecting tube through the heating lid as the liquid level rose. The droplets flowed to the flow-focusing structure through channel A, continuously driven by the analysis oil, as shown in Fig. 2(H). Meanwhile, the remaining generation oil in the reservoir was pressured into the flow-focusing structure under the pressure of 60 kPa to be used as the shearing oil. The oil shearing action reorganized the droplets in an orderly manner at specific intervals for fluorescence readout. The droplets are fluorescently imaged by laser beam at the spot about 4 mm downstream from the flow-focusing structure.

Characterization of droplet generation

In ddPCR analysis, both droplet size and consistency influence the accuracy of the results. Moreover, the throughput of analysis is affected by the time consumed for droplet generation. We studied the droplet size, consistency, and droplet generation frequency at different pressure parameters using the chip on our platform. Furthermore, we observed that the droplet-to-oil volume ratio varied with different pressure parameters. As shown by the thermodynamic simulation results in Fig. S4,† the larger γ_{do} is, the faster the droplet temperature reaches the set value. Therefore, we studied the γ_{do} under various pressure parameters. In the experiment, sample pressure varied from 4 to 24 kPa in increments of 4 kPa. Oil pressure was adjusted from half to twice the sample pressure. Ultimately, we determined the optimal sample and oil pressure parameters using our chip. Additionally, we generated droplets in six chips, then surface-treated them following the steps:

1. The hydrophobic agent of 2% v/v FOTS dissolved in engineered fluid is prepared.
2. The hydrophobic agent is added to the chip with a pipette, ensuring that it reaches each microchannel.
3. Bake the chip at 80 °C for more than 12 hours to ensure that the agent in the microchannels is completely dry.

The droplet generation procedures are repeated. Finally, we compared the droplet size, consistency, and average size consistency among these chips.

Effects of the temporary storage bin on droplet-to-oil volume ratio

As illustrated in Fig. S4,† having less oil in the collecting tube brings the droplets closer to the thermal cycler, thereby improving thermal cycle performance. To verify the optimization of the temporary storage bin for the droplet-to-oil volume ratio, experiments were conducted using different volume samples were for droplet generation, both with and without the temporary storage bin. Each experiment was repeated three times, and the generation process was recorded.

Thermal cycle performance optimization

To enhance thermal cycle performance, we utilized a high-power Peltier and a pure copper heating base with a thermal conductivity of 386.4 W m⁻¹ K⁻¹. Additionally, we conducted calibration of the temperature sensor. Moreover, to account for the delay between the Peltier temperature and the temperature inside the collecting tube, we developed a temperature model. This model uses a product of a first-order inertia element and a pure time delay element, as described in eqn (2):

$$G(s) = G_s(s)e^{-\tau s} = \frac{K_s}{T_s s + 1} e^{-\tau s} \quad (2)$$

where s represents the complex frequency variable in the Laplace domain, K_s represents the gain coefficient, T_s represents the time coefficient, τ represents the delay time constant, and $G(s)$ is the transfer function of the thermal cycle system, which is the ratio of the Laplace transform of the output (the temperature in the collecting tube) to the input (voltage or power applied to the Peltier). We obtained the coefficients using the ascending curve. Following this model, we optimized the thermal control algorithm, where the Smith predictor was used to compensate for time delay, as described below:

$$G_P(s) = G_s(s)(1 - e^{-\tau s}) \quad (3)$$

where $G_P(s)$ represents the transfer function of the Smith predictor, connected in parallel with the controller to form a negative feedback loop. The principle of the Smith predictor for thermal cycle performance optimization is illustrated in Fig. S5.†

Evaluation of the fluorescence readout performance

During readout, two laser diodes were turned on. The optical lenses and dichroic mirrors merged two laser beams of different wavelengths and made their focal spots converged at the same spot. The focal spot was irradiated onto the droplet by adjusting the position of the laser sources. When a droplet passed through the focal spot, the fluorescent substances inside were excited to emit fluorescence signals. These signals were converted into electrical signals by APD detectors through the optical elements and subsequently

sampled and analyzed by a data acquisition card. To minimize the device's size, we adopted an optical path where both lasers and detectors were placed on the same side. The fluorescence was separated from the laser beam through the optical elements. A lens was installed in front of the detector to improve the fluorescence receiving efficiency, thereby enhancing the SNR.

To evaluate quantification performance, we prepared 24 samples (20 μL each). The concentrations of HER2 and CEP17 genes in each of the three replicates were 0, 0.5, 1, 5, 10, 50, 100, and 500 copies per μL , respectively, achieved by dilution. The ddPCR analysis was performed on the platform. Finally, the concentrations of HER2 and CEP17 genes were calculated from the number of negative and positive droplets and droplet size in each sample using Poisson distribution, as follows:

$$c = -\frac{\ln(1 - N_p/N)}{V_d} \quad (4)$$

where c represents the calculated concentrations of the target genes, N_p represents the number of positive droplets, N

represents the total number of droplets, and V_d represents the volume of a single droplet.

Results and discussions

The characterization of droplet generation

The results of the droplet generation experiment are presented in Fig. 3. The process of droplet generation was recorded by a high-speed camera at an appropriate frame rate to ensure a clear and bright line of sight while catching all the droplets, as depicted in Fig. 3(A). Droplets are formed somewhere after the flow-focusing structure and are equidistantly arranged. As depicted by the curves in Fig. 3(B), when the sample pressure is fixed, the generation frequency gradually increases with the rise in oil pressure. As expected, a high generation frequency improves analysis efficiency. However, as Fig. 3(C) indicates, higher oil pressure results in a lower γ_{do} , thereby increasing the consumption of generation oil. An excessively high γ_{do} was noticed when the oil-to-sample pressure ratio is small, as the fluid is in an

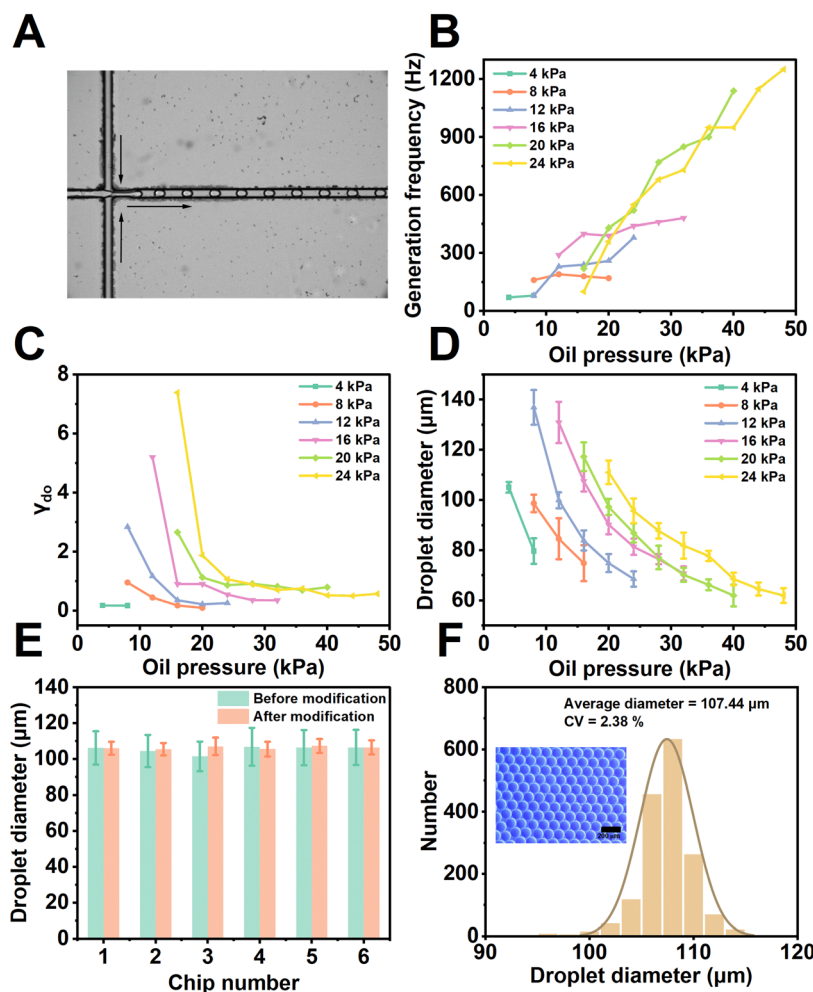


Fig. 3 The results of droplet generation. P_s represents sample pressure in figures (B–D). (A) A high-speed camera captured the process of droplet generation. (B) Generation frequency at different parameters. The frame rate was 20 000 fps. (C) Droplet-to-oil volume ratio (γ_{do}) at different parameters. (D) Droplet diameters at different parameters. (E) Results of droplet generation in six chips with and without surface treatment (16 kPa, 16 kPa). (F) The statistical result of 1641 droplets, and one of the droplet images taken by the microscope (16 kPa, 16 kPa).

unstable state at this time. Similarly, droplet size decreases nonlinearly with increasing oil pressure, and we found that the decreasing trend of the droplet size gradually leveled off, according to Fig. 3(D). In conclusion, we chose parameters of 16 kPa for both the sample and oil pressure to achieve a high generation frequency, a high γ_{do} , and suitable droplet size for readout.

The results of droplet generation in the chips with and without surface treatment are shown in Fig. 3(E). We can see that the droplet sizes are similar in two sets of experiments. However, droplet sizes are less consistent when droplets were generated in the chip without surface treatment. Conversely, the size consistency of the droplets generated in the treated chips is significantly improved. Furthermore, we calculated that the CVs of the average diameters of the droplets generated in the chips with and without surface treatment are 0.86% and 2.20%, respectively, indicating improved consistency of the average droplet size among chips after surface treatment.

We conducted the droplet generation experiment on a chip with surface treatment and counted the size of 1641 droplets. The statistical result is shown in Fig. 3(F). We calculated that the average diameter of the 1641 droplets is 107.44 μm and the consistency of the droplet diameters is good, with a coefficient of variation (CV) of 2.38%.

The performance of the temporary storage bin

Fig. 4(A) and (B) show the pressure and liquid volume changes in the collecting tube during droplet generation with and without a temporary storage bin. The sample pressure and generation oil pressure were both set to 16 kPa. Droplets and generation oil started to enter the collecting tube at 97 seconds and 30 seconds, with and without a temporary storage bin. At the time of sample depletion, the sample pressure dropped slowly. The sample pressure dropped to 15.8 kPa when all the droplets entered the collecting tube, indicating the completion of droplet generation. The droplet generation time with and without a temporary storage bin was 132 seconds and 121 seconds, respectively, demonstrating that the temporary storage bin did not affect the time required for droplet generation. We found from the figure that the γ_{do} in the experiment with a temporary storage bin is more significant than the result without a temporary storage bin. Subsequently, the oil pressure dropped to 15.8 kPa, and the sample pressure dropped to 15.0 kPa. At this point, the generation oil was depleted. Comparing subfigures (iii) and (iv) of Fig. 4(B) reveals that a substantial volume of oil enters the collecting tube due to the limited capacity of the temporary storage bin. This observation suggests that the completion of droplet generation occurs when the sample

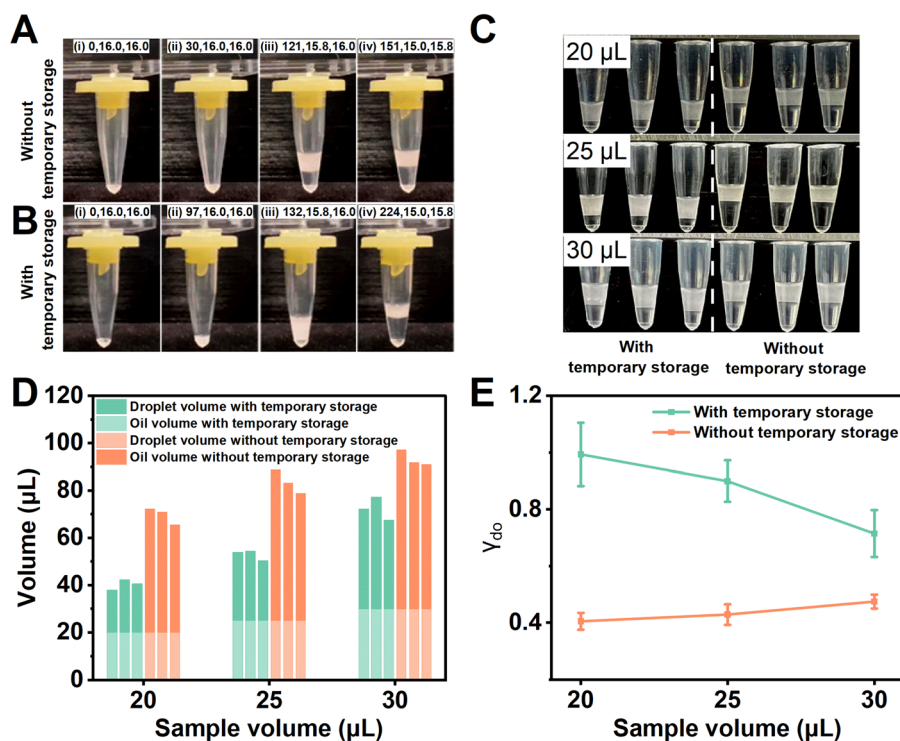


Fig. 4 The experimental results of temporary storage bin characterization with and without a temporary storage bin integrated into the rotary valve. (A) The record of the liquid in the collecting tube during droplet generation without a temporary storage bin. (B) The record of the liquid in the collecting tube during droplet generation with a temporary storage bin. The subtitles in Fig. 4(A) and (B) follow the format: (number, time (s), sample pressure (kPa), oil pressure (kPa)). (C) The sample and oil composition in collecting tubes when the sample volume is 20 μL , 25 μL , and 30 μL , respectively. (D) Droplet volume and oil volume in each collecting tube. (E) The average droplet-oil volume ratio when the sample volume is 20 μL , 25 μL , and 30 μL , respectively.

pressure falls to 15.8 kPa, facilitating the acquisition of a sample with an optimal water-to-oil volume ratio. Therefore, we regard the time point when the sample pressure falls to 15.8 kPa as the sign of the completion of the droplet generation in a normal ddPCR analysis.

We found from Fig. 4(C) that the oil volume with a temporary storage bin is less than that without a temporary storage bin in each set of experiments. We calculated the droplet and oil volumes in each collecting tube, as shown in Fig. 4(D), which shows less generation oil consumption with a temporary storage bin than without a temporary storage bin. Furthermore, the γ_{do} with a temporary storage bin is about 2.5 to 1.5 times that without a temporary storage bin and declines, as the sample volume increases as shown in Fig. 4(E). All the above results show that the temporary storage bin is helpful for improving the γ_{do} , which is beneficial for the thermal cycle performance.

Thermal cycle performance after optimization

Fig. 5(A) displays the internal structure of the thermal cycler. There is a pure copper heating base, a Peltier, and a cooling fin from top to bottom joined together with silicone grease. We drove the Peltier with a constant power of 4 W, and the initial temperature was 60 °C. The measured curve in Fig. 5(B) shows that it reaches stability at about 83.3 °C, and the parameters of the transfer function can be calculated with the Cohen–Coon formula as eqn (5):

$$\begin{cases} K_s = \Delta U / \Delta R \\ T_s = 1.5(t_{0.632} - t_{0.28}) \\ \tau = 1.5(t_{0.28} - 1/3t_{0.632}) \end{cases} \quad (5)$$

where ΔU represents the output increment, ΔR represents the input increment, and $t_{0.28}$ and $t_{0.632}$ represent the corresponding time when the output is 28% and 63.2%, respectively. We obtained the parameters from the measured curve, and the transfer function is as follows:

$$G(s) = \frac{5.81}{853.5s + 1} e^{-9.5s} \quad (6)$$

the ‘Model curve’ in Fig. 5(B) is the step response of the model, which is consistent with the measured curve. This transfer function can describe the dynamic characteristics of the thermal cycle system. Moreover, we calibrated the temperature sensor and obtained the result with a good linearity ($R^2 = 0.9995$), as shown in Fig. 5(C). We calibrated the temperature value as follows:

$$t_r = 1.07498t_s - 1.5988 \quad (7)$$

where t_s represents the temperature value obtained from the sensor, and t_r represents the real temperature. Fig. 5(D) shows the temperature curve before optimization, and the target temperature could not be reached during each thermal cycle, specifically during denaturation.

We designed the digital Smith predictor in the program according to the model and corrected the parameters with the temperature sensor calibration result for more accurate

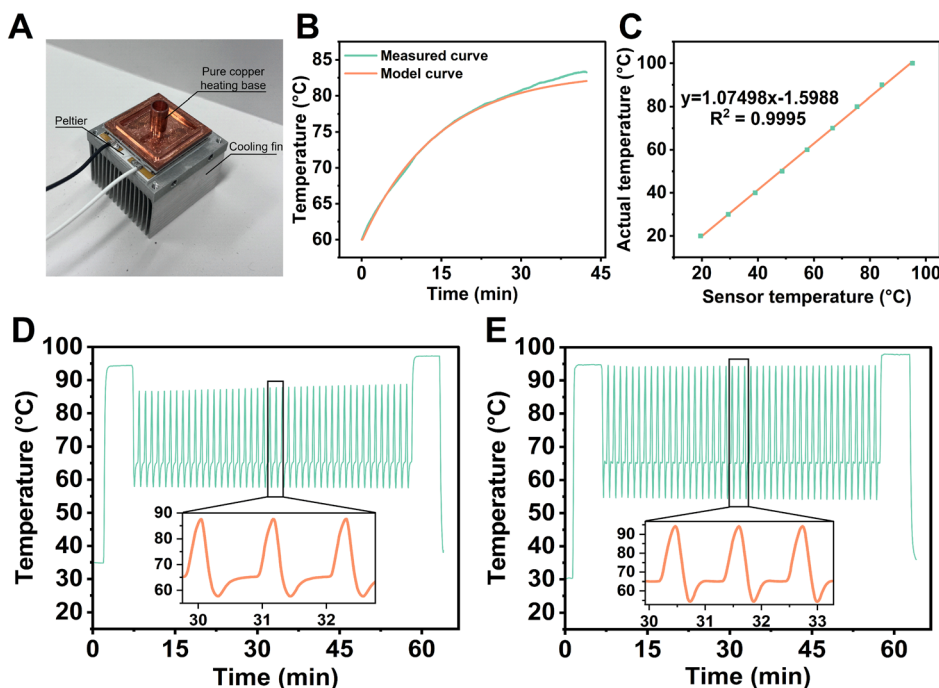


Fig. 5 The results of thermal cycle performance optimization. (A) The internal structure of the thermal cycler. (B) The ascending curve and the step response curve. (C) The temperature sensor calibration curve. (D) The thermal cycle curve before optimization. (E) The thermal cycle curve after optimization.

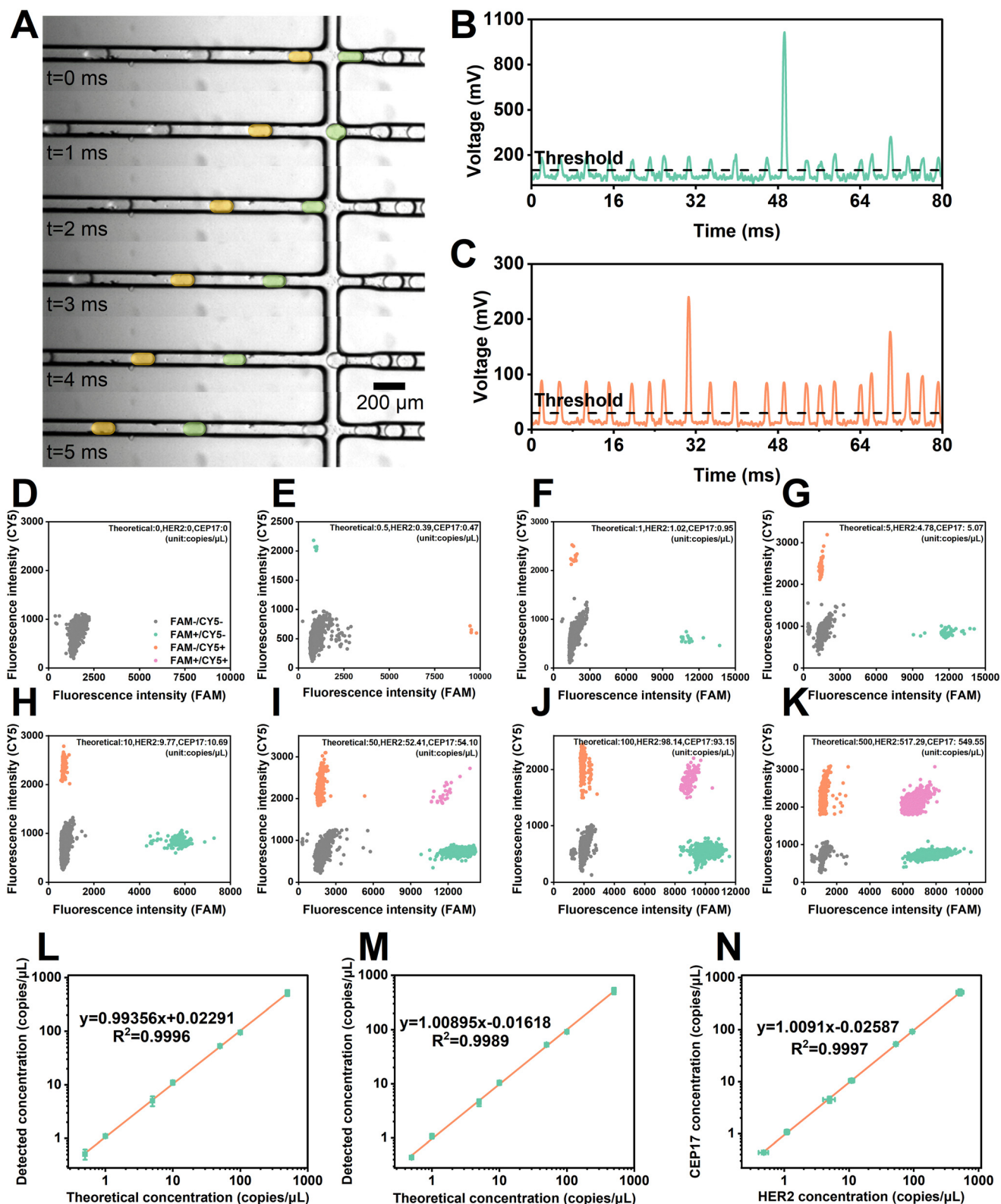


Fig. 6 Readout performance and ddPCR quantification results. (A) Movement of droplets in the microchannel during reflux readout. The frame rate was 20 000 fps. (B) Voltage waveforms of the FAM channel. (C) Voltage waveforms of the CY5 channel. (D–K) 2D fluorescence intensity of the FAM channel and the CY5 channel with concentrations of 0, 0.5, 1, 5, 10, 50, 100, and 500 copies per μL respectively. (L) The linear fitting curve of quantification results for the HER2 gene. (M) The linear fitting curve of quantification results for the CEP17 gene. (N) The linear fitting curve of detected HER2 and CEP17 concentrations.

temperature control. The results are shown in Fig. 5(E), and all the target temperatures are reached within a deviation of ± 0.5 °C. Moreover, both amplifications took 64 minutes, showing that we improved temperature accuracy without compromising time.

Evaluation of ddPCR readout performance

Before the experiment, the laser diodes' position and height were adjusted to place the focal spot in the microchannel. During readout, we drove the analysis oil with a bit higher pressure than generation oil. Otherwise, droplets could not cross the flow-focusing structure due to the obstruction by generation oil. Here, we used a 70 kPa pressure to drive the analysis oil and a 60 kPa pressure to drive the generation oil. The movement of droplets in the microchannel is shown in Fig. 6(A). Before the flow-focusing structure, droplets were densely arranged and moved at a low speed. In contrast, droplets accelerated and queued up evenly at regular intervals after passing through the flow-focusing structure without coalescing or breaking. We used an oscilloscope to capture the waveforms of two channels, as shown in Fig. 6(B) and (C). After the threshold is determined using the method shown in Fig. S6,† the peak voltage signal of each droplet can be sensitively recorded. The relative fluorescence intensity ratios of positive and negative droplets are about 6 and 3 in the FAM channel and the CY5 channel, respectively. It helps to distinguish the 'positive' and 'negative' droplets, improving the accuracy of our platform.

We counted the positive droplet numbers and calculated the concentrations following eqn (4). And the results are listed in Tables 1 and 2. The copy number (K) can be calculated by multiplying the concentration (c) by the sample volume (V_s). The 2D fluorescence intensities of one group are shown in Fig. 6(D–K). Scatter plots form clear clusters in each result. The limit of blank (LOB) and limit of detection (LOD) are calculated as shown in eqn (8) and (9).²²

$$\text{LOB} = \begin{cases} 0, \Lambda_{\text{FP}} = 0 \\ 1, \Lambda_{\text{FP}} \leq 0.05 \\ \Lambda_{\text{FP}} + 1.645\sqrt{\Lambda_{\text{FP}}} + 0.8, \Lambda_{\text{FP}} > 0.05 \end{cases} \quad (8)$$

$$\text{LOD} = \begin{cases} 3, \Lambda_{\text{FP}} = 0 \\ 5, \Lambda_{\text{FP}} \leq 0.05 \\ \frac{1}{4} \left(1.645 + \sqrt{1.645^2 + 4\text{LOB}} \right), \Lambda_{\text{FP}} > 0.05 \end{cases} \quad (9)$$

where Λ_{FP} represents the false positive droplet number in negative samples. Λ_{FP} is 0 because no false positive droplets are detected in negative samples. Therefore, the LOB is 0 copies, and the LOD is 3 copies.

The linear fitting curves of HER2 and CEP17 gene concentration results are plotted in Fig. 6(L) and (M), respectively. High coefficients of determination were observed ($R^2 = 0.9996$ for FAM and $R^2 = 0.9989$ for CY5), indicating good linear relationships in the gradient quantification analysis. The ratio of HER2 to CEP17 is used to determine whether the breast cancer is HER2-positive or HER2-negative.²⁴ Fig. 6(N) demonstrates strong linearity between the detected concentrations of HER2 and CEP17, with a slope (HER2:CEP17 ratio) of 1.0091 and an R^2 of 0.9997, indicating consistent HER2:CEP17 ratios across multiple sample dilutions.

Clinically, there are generally two ways to determine breast cancer using digital PCR:

1. The measurement is conducted using circulating tumor DNA (ctDNA) in the peripheral blood. A volume of 5 mL of blood is processed to isolate 2 mL of plasma. Following lysis, extraction, and elution, a total of 20 μL of product is obtained. Subsequently, 1 μL of this product is utilized for ddPCR analysis.

2. Measurement is made using tumor tissue sections. Usually, 40 μL of DNA is extracted from five breast cancer tumor sections, each 10 microns thick. Subsequently, 10 ng of the DNA is utilized for ddPCR analysis.

In our tests (ESI 3†), the minimum copy numbers of HER2 and CEP17 are 105 and 115 copies, respectively, within the 1 μL product among 24 peripheral blood samples. The minimum copy number of HER2 is about 123 copies, and that of CEP17 is 101 copies in 100 tumor tissue samples. The copy numbers in the peripheral blood and the tumor tissue sections are greater than the LOD of our ddPCR platform. As Suhong Xie, *et al.* reported, a HER2:CEP17 ratio ≥ 1.3 was defined as HER2-positive amplification, and a HER2:CEP17

Table 1 Quantification results of the HER2 gene (R = replicate, SD = standard deviation)

Theoretical concentration (copies per μL)	Quantified number of positive droplets			Detected concentration (copies per μL)				
	R1	R2	R3	R1	R2	R3	Mean	SD
0	0	0	0	0	0	0	0	0
0.5	5	8	7	0.39	0.54	0.52	0.51	0.11
1	15	15	18	1.02	1.08	1.20	1.10	0.09
5	67	52	85	4.78	4.11	6.16	5.02	1.05
10	138	129	152	9.77	11.68	11.57	11.01	1.07
50	598	697	569	52.41	53.80	52.40	52.87	0.81
100	1236	1156	1169	98.14	94.49	91.86	94.83	3.15
500	5065	5439	5762	517.29	452.41	584.52	518.07	66.06

Table 2 Quantification results of the CEP17 gene

Theoretical concentration (copies per μL)	Quantified number of positive droplets			Detected concentration (copies per μL)				
	R1	R2	R3	R1	R2	R3	Mean	SD
0	0	0	0	0	0	0	0	0
0.5	6	6	6	0.47	0.40	0.44	0.44	0.03
1	14	16	17	0.95	1.15	1.14	1.08	0.11
5	71	48	65	5.07	3.79	4.71	4.52	0.66
10	151	104	149	10.69	9.41	11.34	10.48	0.98
50	617	683	560	54.10	52.71	51.56	52.79	1.27
100	1175	1132	1138	93.15	92.47	89.35	91.66	2.03
500	5031	5272	5652	549.55	436.49	571.17	519.07	72.32

ratio <1.3 was defined as a HER2-negative amplification using ddPCR.²⁵ Therefore, the sample with a HER2:CEP17 ratio of 1.0091 in this experiment is defined as a HER2-negative breast cancer. The experimental results show that the concentrations of HER2 and CEP17 detected were in high concordance with their theoretical values on our ddPCR platform. Additionally, our ddPCR platform exhibits good linearity, low limit of detection, and high consistency in HER2:CEP17 ratio calculations. Therefore, our ddPCR platform can be used to determine whether the breast cancer is HER2-negative or HER2-positive.

Conclusions

ddPCR has been proven to have advantages in DNA absolute quantification applications. Moreover, it provides significant advantages in equipment miniaturization, low reagent consumption, process automation, and operational flexibility by combining microfluidics with ddPCR technology. According to previous studies and existing commercial products, achieving automated DNA quantification analysis with the ddPCR platform within a single chip is challenging. In this paper, we developed a ddPCR platform based on a microfluidic chip with a dual-function flow-focusing structure that enables droplet generation and readout at the same flow-focusing structure by switching the rotary valve angle. The microfluidic chip's dual-function flow-focusing structure not only reduces its size but also facilitates the sample-to-result function in ddPCR analysis. Automated ddPCR analysis can be carried out on our platform. To assess the droplet generation performance, we studied the characteristics of droplet generation and the performance of the temporary storage bin. We generated the droplets with an average diameter of 107.44 μm and a CV of 2.38%. At the same time, high-performance thermal cycling was achieved through improvements of the droplet-to-oil volume ratio of the sample, the integrated heating lid, the pure copper heating base, and the temperature-controlling algorithm. We implemented reflux readout and conducted gradient quantitative analysis of the HER2 (FAM) and CEP17 (CY5) genes. The resulting fitting curves exhibited coefficients of determination of 0.9996 and 0.9989, respectively, demonstrating our platform's high linearity in DNA absolute quantification. Strong linearity was obtained between the

detected concentrations of HER2 and CEP17, with a slope (HER2:CEP17 ratio) of 1.0091 and an R^2 of 0.9997, indicating consistent HER2:CEP17 ratios across multiple sample dilutions. The quantitative analysis results, their dynamic range, and the HER2:CEP17 ratio consistency using our ddPCR platform align with the requirements for breast cancer assessment and therapy. The experimental results show that our ddPCR platform characterized by automated analysis, portability, stable droplet generation, high-efficiency amplification, realization of the sample-to-result function based on dual-function flow-focusing structure, and accuracy absolute quantification. The ddPCR platform holds significant potential for clinical diagnosis applications, promising advancements in ddPCR analysis.

Author contributions

Xiaoliang Zhang: methodology, validation, formal analysis, investigation, data curation, writing – original draft, writing – review & editing; Shun Wang: conceptualization, methodology, formal analysis, investigation, data curation, writing – original draft, writing – review & editing; Jinxian Wang: methodology, conceptualization, resources; Xiaojie Sun: methodology, validation; Jinbing Xue: resources; Zhenya Wang: methodology, validation; Tianhang Yang: methodology, formal analysis, writing – review & editing; Liangfei Weng: resources; Bidou Wang: supervision, project administration; Gangyin Luo: conceptualization, supervision, project administration, funding acquisition.

Conflicts of interest

There are no conflicts to declare.

Acknowledgements

We thank the CAS Engineering Laboratory for *In Vitro* Diagnostic (20210419115032678) and Suzhou Pilot Project of Basic Research (SJC2022015) for support.

Notes and references

- 1 A. Alanio, A. Sturny-Leclere, M. Benabou, N. Guigue and S. Bretagne, *J. Microbiol. Methods*, 2016, **127**, 160–163.

- 2 J. Madic, C. Jovelet, J. Lopez, B. Andre, J. Fatien, I. Miran, A. Honore, L. Mezquita, B. Besse, L. Lacroix and M. Droniou, *Oncotarget*, 2018, **9**, 37393–37406.
- 3 Y. H. Zhang and H. R. Jiang, *Anal. Chim. Acta*, 2016, **914**, 7–16.
- 4 C. W. Kuo and A. M. Smith, *Acc. Chem. Res.*, 2023, **56**, 1031–1042.
- 5 B. Vogelstein and K. W. Kinzler, *Proc. Natl. Acad. Sci. U. S. A.*, 1999, **96**, 9236–9241.
- 6 R. Kanagal-Shamanna, *Clinical Applications of PCR*, 3rd edn, 2016, vol. 1392, pp. 43–50.
- 7 K. R. Sreejith, C. H. Ooi, J. Jin, D. V. Dao and N. T. Nguyen, *Lab Chip*, 2018, **18**, 3717–3732.
- 8 J. Shen, J. Zheng, Z. Li, Y. Liu, F. Jing, X. Wan, Y. Yamaguchi and S. Zhuang, *Lab Chip*, 2021, **21**, 3742–3747.
- 9 C. Y. Wei, C. Z. Yu, S. S. Li, J. Y. Meng, T. J. Li, J. M. Cheng and J. W. Li, *Sens. Actuators, B*, 2022, **371**, 132473.
- 10 J.-Y. Kim, S.-W. Cho, D.-K. Kang, J. B. Edel, S.-I. Chang, A. J. deMello and D. O'Hare, *Chem. Commun.*, 2012, **48**, 9144–9146.
- 11 J. S. Barea, J. Lee and D.-K. Kang, *Micromachines*, 2019, **10**, 412.
- 12 Z. H. Li, B. L. Zhang, D. Dang, X. L. Yang, W. G. Yang and W. F. Liang, *Sens. Actuators, A*, 2022, **344**, 113757.
- 13 B. J. Hindson, K. D. Ness, D. A. Masquelier, P. Belgrader, N. J. Heredia, A. J. Makarewicz, I. J. Bright, M. Y. Lucero, A. L. Hiddessen, T. C. Legler, T. K. Kitano, M. R. Hodel, J. F. Petersen, P. W. Wyatt, E. R. Steenblock, P. H. Shah, L. J. Bousse, C. B. Troup, J. C. Mellen, D. K. Wittmann, N. G. Erndt, T. H. Cauley, R. T. Koehler, A. P. So, S. Dube, K. A. Rose, L. Montesclaros, S. Wang, D. P. Stumbo, S. P. Hodges, S. Romine, F. P. Milanovich, H. E. White, J. F. Regan, G. A. Karlin-Neumann, C. M. Hindson, S. Saxonov and B. W. Colston, *Anal. Chem.*, 2011, **83**, 8604–8610.
- 14 S. H. Zhao, Z. M. Zhang, F. Hu, J. J. Wu and N. C. Peng, *Analyst*, 2021, **146**, 1559–1568.
- 15 D. Pekin, Y. Skhiri, J.-C. Baret, D. Le Corre, L. Mazutis, C. Ben Salem, F. Millot, A. El Harrak, J. B. Hutchison, J. W. Larson, D. R. Link, P. Laurent-Puig, A. D. Griffiths and V. Taly, *Lab Chip*, 2011, **11**, 2156–2166.
- 16 M. Nie, M. Zheng, C. Li, F. Shen, M. Liu, H. Luo, X. Song, Y. Lan, J.-Z. Pan and W. Du, *Anal. Chem.*, 2019, **91**, 1779–1784.
- 17 C. Y. Wei, C. Z. Yu, S. S. Li, J. Y. Meng, T. J. Li, J. M. Cheng, F. Pan and J. W. Li, *Anal. Chem.*, 2022, **94**, 3939–3947.
- 18 Y. L. Ren, J. C. Ji, H. Q. Zhang, L. Cao, J. Hu, F. Xu and Z. D. Li, *Lab Chip*, 2023, **23**, 2521–2530.
- 19 X. Cui, L. Wu, Y. Wu, J. H. Zhang, Q. Zhao, F. X. Jing, L. Yi and G. Li, *Anal. Chim. Acta*, 2020, **1107**, 127–134.
- 20 F. Schlenker, E. Kipf, N. Borst, N. Paust, R. Zengerle, F. von Stetten, P. Juelg and T. Hutzenlaub, *Processes*, 2021, **9**, 97.
- 21 H. Yang, J. Yu, L. Jin, Y. Zhao, Q. Gao, C. Shi, L. Ye, D. Li, H. Yu and Y. Xu, *Analyst*, 2023, **148**, 239–247.
- 22 X. R. Zhu, B. X. Liu, S. S. Su, B. Wang, Y. Bai, H. W. Huang, X. B. Liu, X. Cheng, X. H. Wang, L. X. Zhu, W. J. Yang, N. Gao, G. S. Jing and Y. Guo, *Talanta*, 2020, **206**, 9.
- 23 Y. Y. Liu, S. F. Wu, X. H. Shi, F. Mao and X. Zeng, *Front. Oncol.*, 2020, **10**, 985.
- 24 Y. Z. Zhu, D. Lu, M. E. Lira, Q. Xu, Y. Z. Du, J. H. Xiang, M. Mao, H. C. Chung and G. J. Zheng, *Exp. Mol. Pathol.*, 2016, **100**, 287–293.
- 25 S. H. Xie, Y. Wang, Z. Y. Gong, Y. Li, W. T. Yang, G. Y. Liu, J. W. Li, X. Hu, Y. C. Wang, Y. Tong, P. Yuan, Y. R. Si, Y. K. Kang, Y. Mao, X. W. Qi, Y. K. Liu, J. J. Ou, Z. L. Li, X. Pan, Z. Q. Lv, K. Kaji, L. Guo and R. Q. Lu, *J. Cancer*, 2022, **13**, 744–751.